

Pseudo-spectral method using rotated staggered grid for elastic wave propagation in 3D arbitrary anisotropic media

Peng Zou* and Jiubing Cheng

State Key Laboratory of Marine Geology, Tongji University, Shanghai 200092, China

Received November 2016, revision accepted April 2017

ABSTRACT

Staggering grid is a very effective way to reduce the Nyquist errors and to suppress the non-causal ringing artefacts in the pseudo-spectral solution of first-order elastic wave equations. However, the straightforward use of a staggered-grid pseudo-spectral method is problematic for simulating wave propagation when the anisotropy level is greater than orthorhombic or when the anisotropic symmetries are not aligned with the computational grids. Inspired by the idea of rotated staggered-grid finite-difference method, we propose a modified pseudo-spectral method for wave propagation in arbitrary anisotropic media. Compared with an existing remedy of staggered-grid pseudo-spectral method based on stiffness matrix decomposition and a possible alternative using the Lebedev grids, the rotated staggered-grid-based pseudo-spectral method possesses the best balance between the mitigation of artefacts and efficiency. A 2D example on a transversely isotropic model with tilted symmetry axis verifies its effectiveness to suppress the ringing artefacts. Two 3D examples of increasing anisotropy levels demonstrate that the rotated staggered-grid-based pseudo-spectral method can successfully simulate complex wavefields in such anisotropic formations.

Key words: Arbitrary anisotropy, Wave propagation, Pseudo-spectral method, Rotated staggered grid.

INTRODUCTION

The numerical modelling of the seismic wave propagation in realistic media is a key element in earthquake and exploration seismology. Several approaches have been developed with different physical model approximations, different complexity levels of the numerical schemes, and different usage of computational resources; see, for example, Carcione *et al.* (2002) for an overview. The finite-difference method (FDM) remains the most popular numerical method for seismic modelling because it is robust and relatively simple to implement, and it offers a good balance between accuracy and efficiency (Moczo *et al.* 2007; Yang *et al.* 2010; Virieux *et al.* 2011; Liu 2013). Other methods such as the pseudo-spectral (Kosloff and Baysal 1982; Sun *et al.* 2016a), finite-element (Eriksson

and Johnson 1991), spectral elements (Komatitsech *et al.* 2000), discontinuous Galerkin (Chung and Engquist 2006; De Basabe *et al.* 2008), finite-volume (Benjemaa *et al.* 2007), and grid methods (Zhang and Liu 1999) are used to various extent in the geophysical community. Wave propagation simulation has attracted a renewed interest mainly because the so-called (acoustic or elastic) full-wave equation approaches have become a fundamental tool in seismic migration and waveform inversion, considering the new challenges in exploration, especially anisotropy (Operto *et al.* 2009; Lisitsa and Vishnevskiy 2010; Bartolo *et al.* 2015; Cheng *et al.* 2016).

The pseudo-spectral method (PSM) (Kosloff and Baysal 1982) we used here is an attractive alternative to the FDM that exploits the fast Fourier transform (FFT) algorithm for computing the spatial derivatives. Its main advantage is that it requires considerably fewer grid points per wavelength to attain any desired accuracy (Fornberg 1987). To simulate

*E-mail: 923458778@qq.com

wave propagation in a realistic earth model, many advances have been made to treat the internal interfaces and general boundaries, including the free-surface and irregular topography, e.g., Fornberg (1988), Carcione (1991), Tessmer (1995), Wang and Takenaka (2001), and Klin *et al.* (2010). Nowadays, the availability of computers with faster interprocessor communication and faster and larger shared memory devices makes the parallelisation of the algorithms based on global differential operators less expensive (Klin *et al.* 2010).

However, the PSM has its own difficulties when solving the first-order elastic wave equations, among which the Nyquist errors and the generation of non-causal ringing artefacts cause serious challenge, particularly in the presence of large abrupt changes in the medium (Kosloff and Baysal 1982). As well known, the use of staggered-grid formulations mitigates these problems (Ozdenvar and McMechan 1996; Correa *et al.* 2002). The most common staggered-grid algorithms apply central-difference operators to the spatial derivative of the velocity–stress wave equations (Virieux 1984). However, the standard staggered grid (SSG) can become unstable when the medium exhibits high contrasts in material properties (Roberstsson 1996) and can only be used to model anisotropy up to orthorhombic media (Komatitsch *et al.* 2000). When the anisotropy level is greater than orthorhombic or when the axis of anisotropy is not aligned with the grid, the straightforward use of the SSG configuration is problematic because of essentially different and complicated representations of Hooke’s law. The implementation of the SSG scheme to general anisotropic media leads to the necessity to interpolate the wavefield, thus increasing numerical dispersion (Igel *et al.* 1995). Another interesting attempt was to decompose the stiffness matrix into aligned and non-aligned parts, with very expensive shift operations used to assist staggering on the non-aligned parts (Bale 2002).

People know that the rotated staggered grid (RSG) (Saenger *et al.* 2000) and the Lebedev grid (LG) (Lisitsa and Vishnevskiy 2010) have good performance for finite-difference modelling in anisotropic media with symmetries lower than orthorhombic. Both grid configurations share the property that all stress components are defined at the same location, as are all velocity components, although velocities and stresses do not coincide. To our knowledge, however, there are few efforts to apply the RSG or LG configuration to pseudo-spectral modelling.

In this study, we propose a PSM using the RSG configuration for simulating elastic wave propagation in 3D arbitrary anisotropic media. We first revisit the PSM using the SSG and its remedy for tackling the constitutive relation

having non-aligned terms. Then we present the methodology of RSG-based pseudo-spectral modelling and compare with alternative approaches, e.g., using the LG configuration. Synthetic examples with increasing anisotropy levels are shown to demonstrate the effectiveness of the RSG-based PSM.

PSEUDO-SPECTRAL METHODS USING STANDARD STAGGERED GRID

To facilitate tackling heterogeneities in the field of medium parameters and implementing the perfectly matched layer boundary condition, we use the first-order elastic wave equations for the pseudo-spectral modelling. Following Carcione (2007), we denote the spatial variables x , y , and z of a right-hand Cartesian system by the indices i , j , $k = 1, 2$ and 3 , respectively. A partial derivative with respect to a variable x_i is denoted by ∂_i , and the first-order time derivatives are denoted by ∂_t . The Einstein convention of repeated indices is used unless otherwise specified.

We express the particle motion equation as

$$\rho \partial_t v_i = \partial_j \tau_{ij} + f_i, \quad (1)$$

in which τ_{ij} and v_i represent the stress and particle velocity components, respectively; ρ is the mass density, and f_i denotes the components of the body force per mass unit. The constitutive relationship (the generalised Hooke’s law) for general anisotropic media is given by

$$\begin{bmatrix} \partial_t \tau_{xx} \\ \partial_t \tau_{yy} \\ \partial_t \tau_{zz} \\ \partial_t \tau_{yz} \\ \partial_t \tau_{xz} \\ \partial_t \tau_{xy} \end{bmatrix} = \begin{bmatrix} C_{11} & C_{12} & C_{13} & C_{14} & C_{15} & C_{16} \\ C_{12} & C_{22} & C_{23} & C_{24} & C_{25} & C_{26} \\ C_{13} & C_{23} & C_{33} & C_{34} & C_{35} & C_{36} \\ C_{14} & C_{24} & C_{34} & C_{44} & C_{45} & C_{46} \\ C_{15} & C_{25} & C_{35} & C_{45} & C_{55} & C_{56} \\ C_{16} & C_{26} & C_{36} & C_{46} & C_{56} & C_{66} \end{bmatrix} \times \begin{bmatrix} \partial_x v_x \\ \partial_y v_y \\ \partial_z v_z \\ \partial_z v_y + \partial_y v_z \\ \partial_z v_x + \partial_x v_z \\ \partial_x v_y + \partial_y v_x \end{bmatrix}, \quad (2)$$

where C_{ij} (using the Voigt notation) denote the components of the stiffness tensor.

PSMs evaluate spatial derivatives by wavenumber multiplication in the Fourier domain (Kosloff and Baysal 1982).

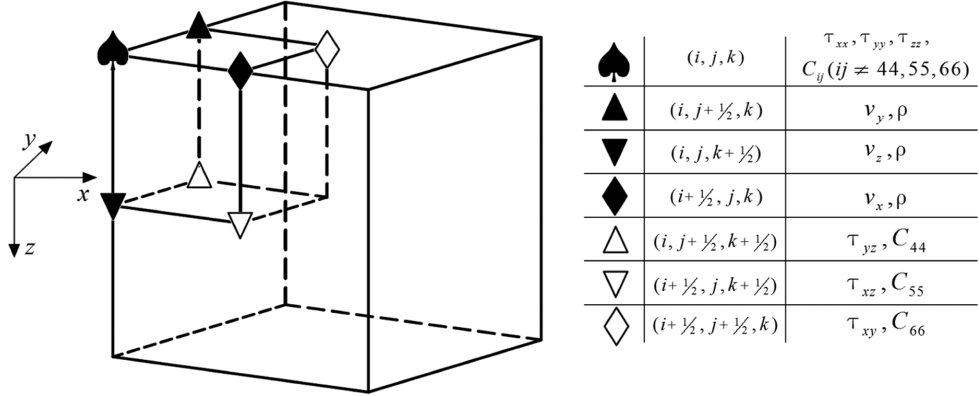


Figure 1 Staggered grid configuration for 3D elastic wave modelling.

For example, the first-order differential in the x -direction can be calculated by

$$D_x \phi = \sum_{k_x=0}^{k_x(N)} ik_x \tilde{\phi}(k_x) \exp(ik_x x), \quad (3)$$

where $\tilde{\phi}$ is the Fourier transform of ϕ and $k_x(N)$ is the Nyquist wavenumber. This formulation automatically achieves the highest theoretically possible accuracy for the spatial differential but suffers from non-causal ringing artefacts due to the discontinuity of spectrum at the Nyquist wavenumber (Mora 1986; Ozdenvar and McMechan 1996). A systematic investigation of this phenomenon is found in Correa *et al.* (2002). Ozdenvar and McMechan (1996) found that the non-causal ringing artefacts can be addressed by using a staggered-grid configuration. The main idea is to calculate spatial derivatives halfway between two regular grid points (Virieux 1984). Therefore, the staggered differential with respect to x can be rewritten as

$$D_x^\pm \phi = \sum_{k_x=0}^{k_x(N)} ik_x \cdot s_x^\pm \cdot \tilde{\phi}(k_x) \exp(ik_x x), \quad (4)$$

where $s_x^\pm = \exp(\pm ik_x \Delta x / 2)$ denotes a forward or a backward phase shift. Similarly, the staggered differentials with respect to y and z need the phase shift operators, i.e., $s_y^\pm = \exp(\pm ik_y \Delta y / 2)$ and $s_z^\pm = \exp(\pm ik_z \Delta z / 2)$, respectively.

Accordingly, Carcione (1999) presented the staggered mesh for a 2D viscoelastic and vertical transversely isotropic (VTI) wave equation. His solution can be straightforwardly extended to three dimensions and used for orthorhombic symmetries aligned with the computational grid. In 3D cases, seven different locations are required to define the stress, strain, and particle velocity components on an elementary cell (see Fig. 1). While the diagonal elements of the stress and strain

tensors are defined at the corner of the cell, the off-diagonal elements are defined at the centre of the cube faces. The components of particle velocity are located halfway between the corners of the cube.

When evaluating the stress-strain relation, it is necessary to sum over a linear combination of the elements of the stiffness tensor and the corresponding elements of the strain tensor. It is challenging to apply the standard staggered-grid scheme to anisotropic media with symmetry lower than orthorhombic (Komatitsch *et al.* 2000). In this context, the stiffness tensor has no special structure. For a finite-difference implementation, some interpolation of the strain components is needed to determine the stress components due to the use of staggered grids (Igel *et al.* 1995). If we calculate the Hooke sum at the points where the diagonal elements of the stress are defined, the off-diagonal elements of the strain have to be interpolated to these locations, whereas the off-diagonal elements of the stress tensor will have to be interpolated to their proper locations. The tapered and truncated interpolation operators induce additional errors in the wave properties (e.g., the phase and group velocities), depending on the symmetry of the anisotropic medium, the orientation of the symmetry axis, the degree of anisotropy, and the interpolation operator.

Because grid staggering can be represented with unitary shift operators for a forward shift and a backward shift along the coordinate axis, an interpolation in the space domain can be replaced by the corresponding phase shift in the wavenumber domain. Accordingly, Bale (2002) suggested decomposing the stiffness matrix into aligned and non-aligned parts: $C_{stag} = C_{ort} + S^+ C_{non} S^-$, with the diagonal matrices S^+ and S^- introduced to assist the staggering on the non-aligned stiffness components (see Appendix A). The shift operations with S^- can be merged into the spectral derivative operator but those with S^+ cannot. This requires many additional fast

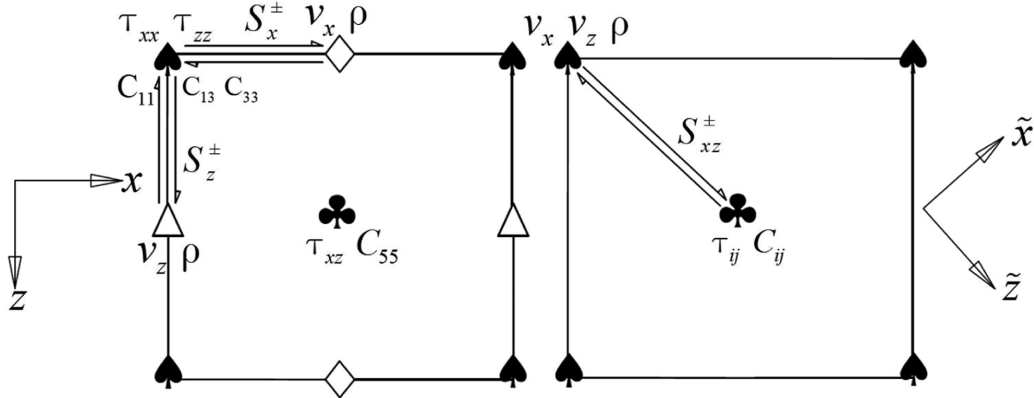


Figure 2 Two-dimensional elementary cells of (left) SSG and (right) RSG. The arrows denote the half-grid shifts along the axes or the diagonal directions.

Fourier transforms to finish the post-multiplication by S^+ and undoubtedly significantly increases the computational costs. As demonstrated by Bale (2002), the unwanted non-causal ringing artefacts are considerably suppressed although the shift operations for the non-aligned parts reintroduce Nyquist discontinuities.

PSEUDO-SPECTRAL METHOD USING THE ROTATED STAGGERED GRID

To avoid multiplying the values of strain component and stiffness coefficient defined at different locations, all stiffness coefficients have to be defined at the same location and the spatial derivatives defined between them are to be differentiated. As well known, the rotated staggered-grid (RSG) configuration proposed by Saenger *et al.* (2000) satisfies all these requirements. This technique is widely used nowadays for finite-difference modelling in great contrast and in general anisotropic media, e.g., Bansal and Sen (2008).

In Fig. 2, we illustrate the RSG configuration for 2D elastic wave modelling, together with the standard staggered-grid (SSG) configuration as a reference. The RSG is based on rotating the system of coordinates such that the spatial derivatives are approximated along artificial (e.g., diagonal) directions and then linearly combined to reconstruct the derivatives in the original coordinate system (Saenger *et al.* 2000). We find that applying the RSG configuration to pseudo-spectral methods (PSMs) has the following advantages. First, if we do not consider the ringing artefacts for the moment, it possesses the same accuracy as the SSG-based PSM due to the sampling theory, as long as their elementary cells have the same sizes. Second, it can suppress the ringing artefacts to an acceptable

level almost with the same computational cost as the SSG-based counterpart.

For pseudo-spectral implementation, the RSG configuration only needs half-grid forward and backward shifts in the diagonal directions (see Fig. 3). Thus, for 3D wave propagation, the RSG-based PSM requires the following phase shifts:

$$s_{xyz}^\pm = e^{\pm i(k_x \Delta x/2 + k_y \Delta y/2 + k_z \Delta z/2)}, \quad (5)$$

for the spatial derivatives in equations (1) and (2). For instance, the derivatives in the x -direction can be calculated using

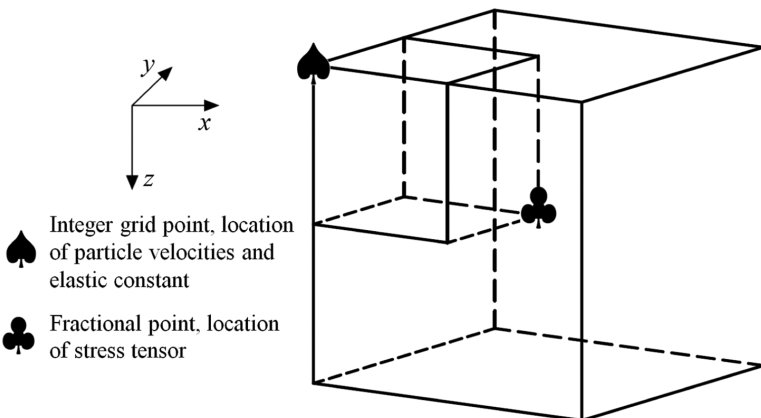
$$\widehat{D}_x^\pm \phi = \sum_{k_x=0}^{k_x(N)} ik_x s_{xyz}^\pm \tilde{\phi}(k_x) \exp(ik_x x). \quad (6)$$

With these spectral derivative operators, we solve the velocity-stress equations using

$$\rho \partial_t v_i = \widehat{D}_i^\pm \tau_{ij} + f_i, \quad (7)$$

and

$$\begin{bmatrix} \partial_t \tau_{xx} \\ \partial_t \tau_{yy} \\ \partial_t \tau_{zz} \\ \partial_t \tau_{yz} \\ \partial_t \tau_{xz} \\ \partial_t \tau_{xy} \end{bmatrix} = \begin{bmatrix} C_{11} & C_{12} & C_{13} & C_{14} & C_{15} & C_{16} \\ C_{12} & C_{22} & C_{23} & C_{24} & C_{25} & C_{26} \\ C_{13} & C_{23} & C_{33} & C_{34} & C_{35} & C_{36} \\ C_{14} & C_{24} & C_{34} & C_{44} & C_{45} & C_{46} \\ C_{15} & C_{25} & C_{35} & C_{45} & C_{55} & C_{56} \\ C_{16} & C_{26} & C_{36} & C_{46} & C_{56} & C_{66} \end{bmatrix} \times \begin{bmatrix} \widehat{D}_x^- v_x \\ \widehat{D}_y^- v_y \\ \widehat{D}_z^- v_z \\ \widehat{D}_z^- v_y + \widehat{D}_y^- v_z \\ \widehat{D}_z^- v_x + \widehat{D}_x^- v_z \\ \widehat{D}_x^- v_y + \widehat{D}_y^- v_x \end{bmatrix}, \quad (8)$$



in which \widehat{D}_y^\pm and \widehat{D}_z^\pm are defined with the same phase shift operators as \widehat{D}_x^\pm in equation (6).

To our interests, the equation of motion only uses forward-shifted spectral derivative operators, whereas the constitutive relation only uses backward-shifted spectral derivative operators. This implies that all the phase shifts can be merged into the spectral derivative operations, and thus, no extra fast Fourier transforms are needed. The RSG spectral derivative operator in equation (6) can be decomposed into two parts: an SSG part $ik_x s_x^\pm$ and a non-SSG part $s_y^\pm s_z^\pm$ in the wavenumber domain. The presence of the non-SSG part reintroduces the Nyquist discontinuities on the k_x axis, similar with the stiffness matrix decomposition-based PSM. Fortunately, the phase jumps across the Nyquist wavenumber are relieved to some extent due to variable scaling by the additional phase shift $s_y^\pm s_z^\pm$. If necessary, application of a wavenumber filter that tapers the spectrum to zero at the Nyquist wavenumbers may be helpful to suppress the residual ringing artefacts.

COMPARISON WITH ALTERNATIVE IMPLEMENTATIONS

We observe that the non-standard staggered-grid (SSG) shift operations may be avoided in theory by defining all components of particle velocity on one staggered grid and all components of stress and strain at another staggered grid. Fortunately, the Lebedev grid (LG)(Lebedev 1964) just satisfies this requirement. Lisitsa and Vishnevskiy (2010) proposed an LG-based finite-difference modelling in 3D anisotropic elasticity, which uses four non-intersecting stress and particle velocity sets. Similarly, as demonstrated in Appendix B, we may extend the LG scheme to pseudo-spectral modelling for arbitrary anisotropic media. Because all the particle velocities and

Figure 3 Rotated staggered grid for 3D elastic wave modelling. Note that particle velocity is defined at the corner and stress is defined at the centre of the cell.

stresses are staggered with this configuration, the non-causal ringing artefacts are avoided for the resultant pseudo-spectral method. However, this scheme has some disadvantages. First, it approximates a greater system of equations possessing 24 characteristics, whereas the elastic wave equation system involves only six characteristics (the rest are “artefacts”). Generally, the artificial solutions are related to the true waves and are determined at all grid points, which makes their identification and elimination rather difficult (Lisitsa and Vishnevskiy 2011). The solutions propagating on different grids become independent when the medium is isotropic, and they are only weakly connected for weak anisotropy (Igel *et al.* 1995). Usually, the elimination of artificial solutions for the LG-based scheme is implemented after the calculation of partial derivatives; therefore, these methods used in LG-based finite-difference methods (FDMs) (Lisitsa and Vishnevskiy 2011) are still suitable for LG-based pseudo-spectral methods (PSMs). Second, compared with the non-staggered PSM, the LG-based PSM requires more than four times of memory requirement and floating-point operations (Lisitsa *et al.* 2012).

It is important to note that the spectral derivative operator is implemented in the wavenumber domain; thus, the accuracy of the PSM is essentially controlled by the discrete grid size according to the Nyquist sampling theory. If we do not consider the ringing artefacts for the moment, all four PSMs possess the same accuracy, as long as their elementary cells have the same size. Therefore, the main part of the computational job of the pseudo-spectral algorithm is devoted to the estimation of the spatial derivatives. This operation implies the executions of two fast Fourier transforms (FFTs) (one forward and one backward, respectively) and one array multiplication. Basically, for 3D general anisotropic media, nine wavefield variables (six stress and three particle velocity

Table 1 The number of FFTs required in every time step and the influence of the non-causal ringing artefacts

Methods	Forward FFTs	Backward FFTs	Total FFTs	Ringing artefacts
PSM	9	18	27	strong
SMD-based PSM	24	39	63	very weak
RSG-based PSM	9	18	27	very weak
LG-based PSM	36	72	108	no

components) need nine forward FFTs and 18 backward FFTs (nine for the motion equation and nine for the constitutive relation) because different directional derivatives are required. Table 1 compares the number of FFTs required in each time step and the influence of the non-causal ringing artefacts. In the most simple case of PSM (without grid staggering), we need nine forward FFTs and 18 backward FFTs. Of course, this implementation leads to strong ringing artefacts in the simulated wavefields. As shown in Appendix A, the stiffness matrix decomposition (SMD)-based staggered-grid PSM has 15 non-aligned terms requiring shift operations to assist staggering between the strain and the stress components. This adds 15 more forward and backward FFTs, respectively. Because some of the stiffness components, e.g., C_{44} , C_{55} , C_{66} , and C_{ij} ($ij \neq 44, 55, 66$), are defined at different locations, six additional backward FFTs are required for the forward and backward shifts to finish the Hooke sum. For the rotated staggered-grid (RSG)-based algorithm, all the phase shifts are merged into the spectral derivative operators; hence, it requires the same number of FFTs as in the non-staggered PSM algorithm. The LG-based staggered-grid PSM requires a total of four sets of the wavefield variables to achieve complete staggering, and all phase shift operations can be merged into the spectral derivative operators (see Appendix B). Hence, this scheme adds three times more FFTs compared with the non-staggered PSM.

EXAMPLES

We will first investigate the accuracy of rotated staggered-grid (RSG)-based pseudo-spectral method (PSM) through a comparison with the alternative implementations on a 2D transversely isotropic (TI) model and then demonstrate its applications to a 3D two-layer horizontal transversely isotropic (HTI) and orthorhombic (ORT) model, with the HTI medium

having non-aligned symmetry axis with the coordinate system, and a homogeneous triclinic model. All comparisons use the same spatial grid spacing to guarantee the same accuracy according to the Nyquist sampling theory. For simplicity, no wavenumber-domain tapering operation is used to handle the residual Nyquist discontinuity. The source used throughout is an explosive point with a Ricker wavelet time function having a central frequency of 30 Hz. All numerical experiments are implemented on the same workstation (Intel(R)/Xeon(R)/X5675 CPU). The convolution perfectly matched layer (Komatitsch and Martin 2007) is used to absorb the reflections from the boundaries of the model.

Two-dimensional transversely isotropic model

We compare the pseudo-spectral algorithms based upon different grid configurations on a 2D two-layer TI model. The first layer is a vertical transversely isotropic (VTI) medium with $V_{p0} = 2500$ m/s, $V_{s0} = 1200$ m/s, $\epsilon = 0.2$, and $\delta = -0.2$, and the second one is a transversely isotropic medium having tilted symmetry axis (TTI) with $V_{p0} = 3600$ m/s, $V_{s0} = 1800$ m/s, $\epsilon = 0.2$, and $\delta = 0.1$, and the tilt angle $\theta = 30^\circ$. A point source is placed at the centre of this model. We simulate elastic wave propagation with a grid size of 10 m and a time step of 1 ms, respectively. Figures 4 and 5 show the snapshots of z -component at 0.4 seconds and the corresponding vertical profiles at the location of $x = 0.81$ km. The non-staggered PSM produces non-causal ringing artefacts (near depths of 0.6 and 2.7 km), but all PSMs using the modified staggered-grid configurations suppress the artefacts very well. Half-grid phase shifts are noticeable between different pseudo-spectral methods (PSMs) because the v_z components are placed at different locations of each grid cell. (For example, as shown in Fig. 2, the v_z component is placed at the middle of the grid edge in the standard staggered-grid (SSG) configuration but at the corner of the elementary cell in the RSG configuration.) It takes CPU times of 71 ms for the non-staggered PSM, and 102, 71, and 140 ms for stiffness matrix decomposition (SMD)-based, RSG-, and LG-based PSMs for one step of extrapolation, respectively. The SMD-based staggered-grid PSM spends substantial CPU time to implement the shift operations required for the terms relating to C_{15} and C_{35} . As shown in equation (A-1), the non-aligned part of the stiffness matrix has more terms requiring such kind of shift operation for 3D general anisotropic models. The increase in the number of fast Fourier transforms (FFTs) for the LG-based PSM significantly reduces its computational efficiency. We observe that the RSG-based scheme obtains comparable results with

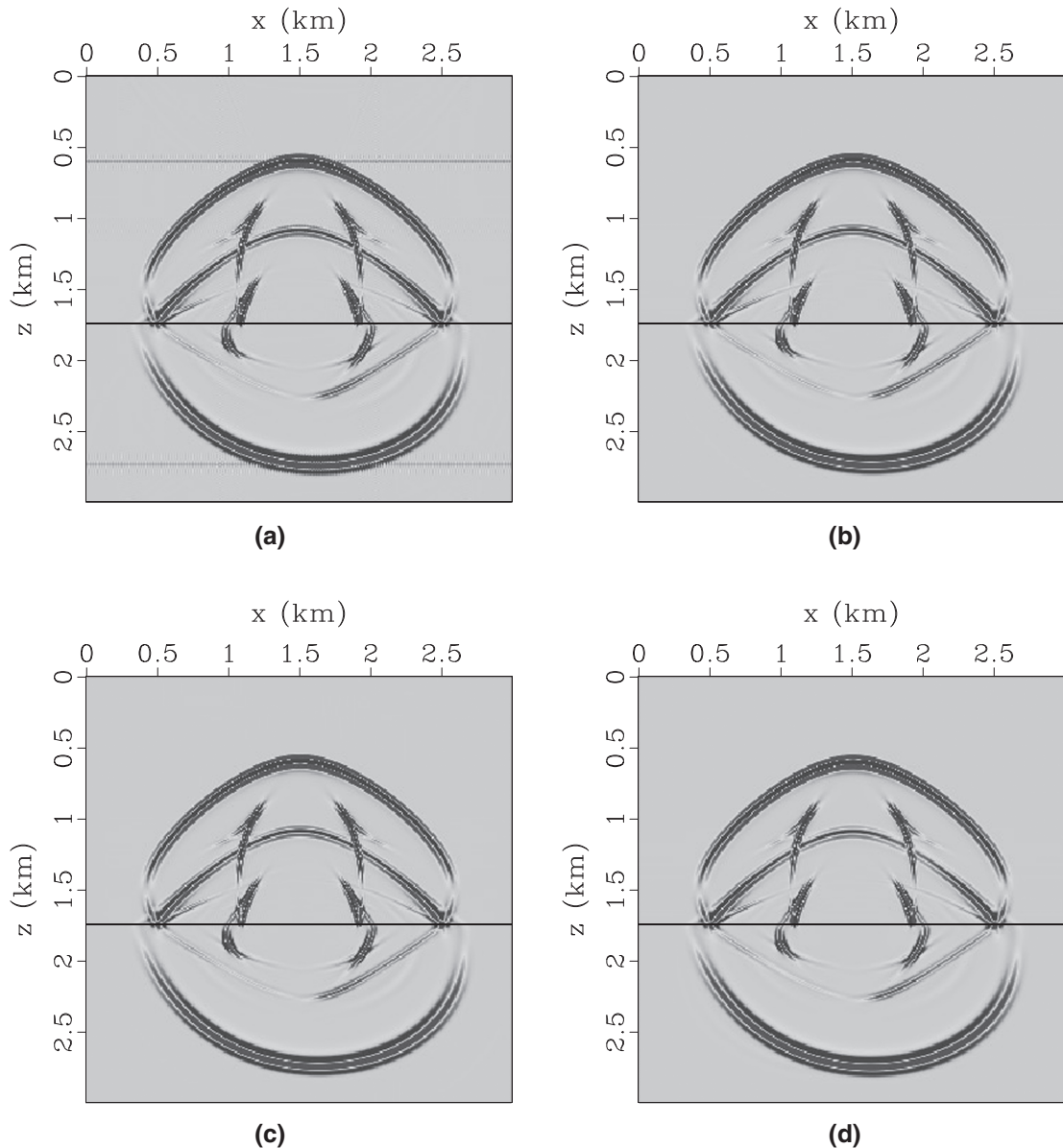


Figure 4 Snapshots of the z -component of the particle velocity field at 0.4 seconds on a 2D two-layer VTI/TTI model: (a) non-staggered PSM; (b) SMD-based PSM; (c) RSG-based PSM; and (d) LG-based PSM.

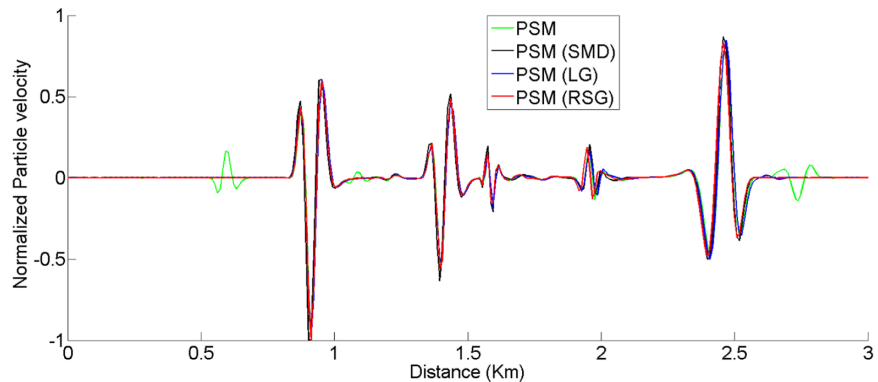
minimum computational resources among the three variants of the staggered-grid PSMs.

Three-dimensional horizontal transversely isotropic and orthorhombic model

Horizontal TI (HTI) and orthorhombic media are the typical effective models used to describe a formation containing parallel vertical fractures. The linear slip model (Schoenberg 1980) can be used to calculate the effective stiffness matrix, given the

background medium and the normal and tangential weaknesses of the fracture system. As demonstrated by Bakulin *et al.* (2000a, b), the effective models of the fractured rocks can be denoted with the Tsvankin parameters. We design a two-layer fractured model to demonstrate the application of the RSG-based PSM for elastic wave modelling. The first layer is an azimuthally rotated HTI medium corresponding to a single vertical fracture set embedded in an isotropic background with $V_p = 3000$ m/s and $V_s = 1800$ m/s. The fracture system has the normal (Δ_N) and tangential (Δ_T) weaknesses of 0.1 and

Figure 5 Vertical profiles extracted from Fig. 4 at the location of $x = 0.81$ Km. The non-causal ringing artefacts produced by the non-staggered PSM presented at 0.6 and 2.7 km. Half-grid phase shifts are noticeable between different PSMs because the v_z components are placed at different locations of each grid cell.



0.2 and an axis of symmetry that is at 30° from the x -axis. The non-zero fracture azimuth lowers the stiffness structure of this medium to monoclinic under the Cartesian coordinate. The second layer is an orthorhombic medium corresponding a set of vertical fractures with an azimuth of 0° in a VTI formation with $V_{p0} = 3600$ m/s, $V_{s0} = 2100$ m/s, $\epsilon = 0.2$, $\delta = 0.1$, and $\gamma = -0.1$. In this case, the fracture weaknesses are $\Delta_N = 0.1$, $\Delta_V = 0.2$, and $\Delta_H = 0.27$.

The simulation of wave propagation is performed within a domain of $4.2 \text{ km} \times 2.56 \text{ km} \times 1.6 \text{ km}$, with a spatial sampling of $\Delta x = \Delta y = \Delta z = 10 \text{ m}$ and a time step of $\Delta t = 0.8 \text{ ms}$. There is a horizontal interface at the depth of 0.93 km. A point source is triggered at $(2.1, 1.28, 0.0)$ km. It takes CPU times of 80 and 192 seconds for the RSG- and SMD-based PSMs for one step of extrapolation, respectively. The time consumption of the LG-based PSM is four times that of the RSG-based PSM and approximately 320 seconds for one step of extrapolation. Figures 6 and 7 show the wavefield snapshots at the time of 0.64 seconds and the seismograms recorded on the surface, respectively. In order to save space, we only display the z -component of the non-staggered PSM for comparison even though the artefacts are obvious in all components. From the RSG-PSM results, we can observe various wave phenomena, including shear-wave splitting, and identify different elastic wave modes in these dispersion-free synthetic wavefields. Artefacts of two types are clearly visible in the non-staggered PSM. The first type is associated with the global ringing nature of the discontinuity of the first-order spectral derivative operator at the Nyquist wavenumber. The second (labelled with arrows) is produced by interaction of the tails of the first derivative operator with the model contrast; it appears to originate on the interface at the same horizontal positions as and simultaneously with the source. The first type of artefact generates the second type at the interface of the media as a secondary source (Ozdenvar and McMechan

1996). Figure 7(d) demonstrates that the amplitudes of the second type of artefacts are of the same order of magnitude as the reflected and converted waves. The ringing artefacts of RSG-PSM are almost invisible even though automatic gain control has been used to highlight the shear waves.

Three-dimensional triclinic model

Finally, we apply the RSG-based PSM to a 3D triclinic medium used by Igel *et al.* (1995). The elastic constants are $C_{11} = 10.0$, $C_{12} = 3.5$, $C_{13} = 2.5$, $C_{14} = -5.0$, $C_{15} = 0.1$, $C_{16} = 0.3$, $C_{22} = 8.0$, $C_{23} = 1.5$, $C_{24} = 0.2$, $C_{25} = -0.1$, $C_{26} = -0.15$, $C_{33} = 6.0$, $C_{34} = 1.0$, $C_{35} = 0.4$, $C_{36} = 0.24$, $C_{44} = 5.0$, $C_{45} = 0.35$, $C_{46} = 0.525$, $C_{55} = 4.0$, $C_{56} = -1.0$, and $C_{66} = 3.0$, where the factor 10^9 N/m^2 is omitted (with density $\rho = 1000 \text{ kg/m}^3$). This material has no physical significance; however, it displays a high anisotropy level and allows us to validate the effectiveness of the algorithm. Figure 8 shows the snapshots of the particle velocity fields at the time of 0.35 seconds. The RSG-PSM obtains dispersion-free simulation results for this anisotropic medium having very low symmetry using the same spatial and temporal sampling as the previous example. The anisotropy of this medium is very strong that the two faster wave modes have very close velocities in some directions; the wavefronts display very complicated kinematic and dynamic features. The first type of ringing artefacts of the non-staggered PSM is still visible in Fig. 8(d) although they die down quickly in homogeneous media and cannot generate the second type of artifacts.

DISCUSSION

Elastic body waves propagate through the earth media as a superposition of P- and S-wave modes. Nowadays, wave mode decoupling becomes not only an essential part of

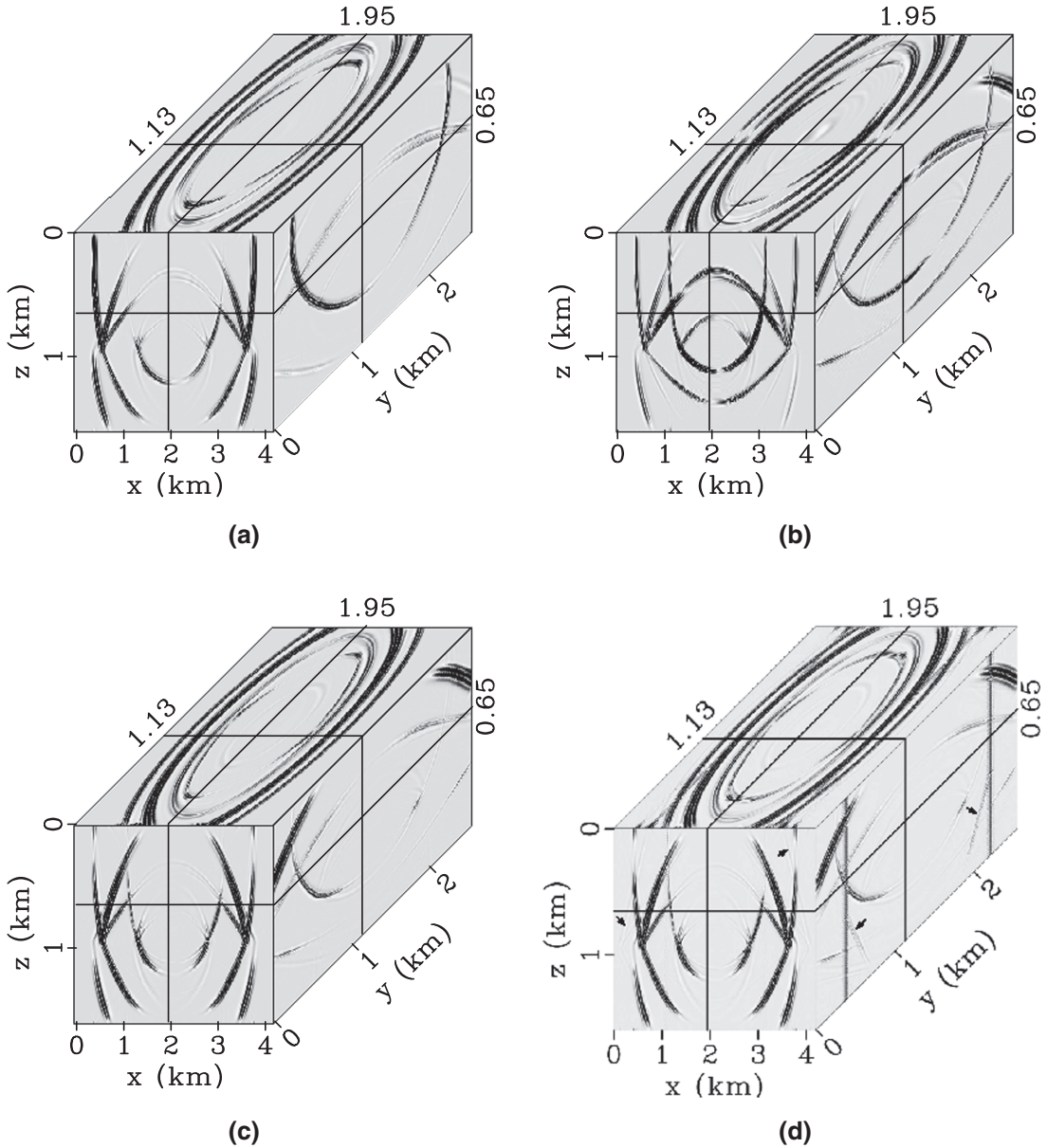


Figure 6 Elastic wavefields in a 3D two-layer monoclinic/orthorhombic model: (a) x -component, (b) y -component, and (c) z -components of RSG-PSM and (d) z -component of the non-staggered PSM. Before azimuthal rotation, the first layer has the HTI parameters of $V_{Pvert} = 2988$ m/s, $V_{S\perp vert} = 1610$ m/s, $\epsilon^{(V)} = -0.0464$, $\delta^{(V)} = -0.1462$, and $\gamma^{(V)} = -0.1$; the second layer has the orthorhombic anisotropic parameters of $V_{p0} = 3578$ m/s, $V_{s0} = 1878$ m/s, $\epsilon_1 = 0.1822$, $\delta_1 = 0.0864$, $\gamma_1 = -0.1364$, $\epsilon_2 = 0.1378$, $\delta_2 = -0.0691$, $\gamma_2 = -0.2091$, and $\delta_3 = -0.0713$, respectively. Global ringing artefacts produced by the non-staggered PSM are clearly visible in the wavefield. Black arrows labelled the second type of artefacts, which are produced by interaction of the global ringing tails with the model contrast.

seismic imaging (Yan and Sava 2008; Wang *et al.* 2016) but also a promising strategy to mitigate parameter trade-offs and speed up the convergence in elastic full-waveform inversion (Wang and Cheng 2016). Note that additional addressment may be required when we decompose the far-field

elastic wave modes from the vector wavefields synthesized using the staggered-grid configurations. For the standard staggered-grid configuration, the particle velocities may not all be located at the same points, hence cannot be directly decomposed using the Helmholtz decomposition theory

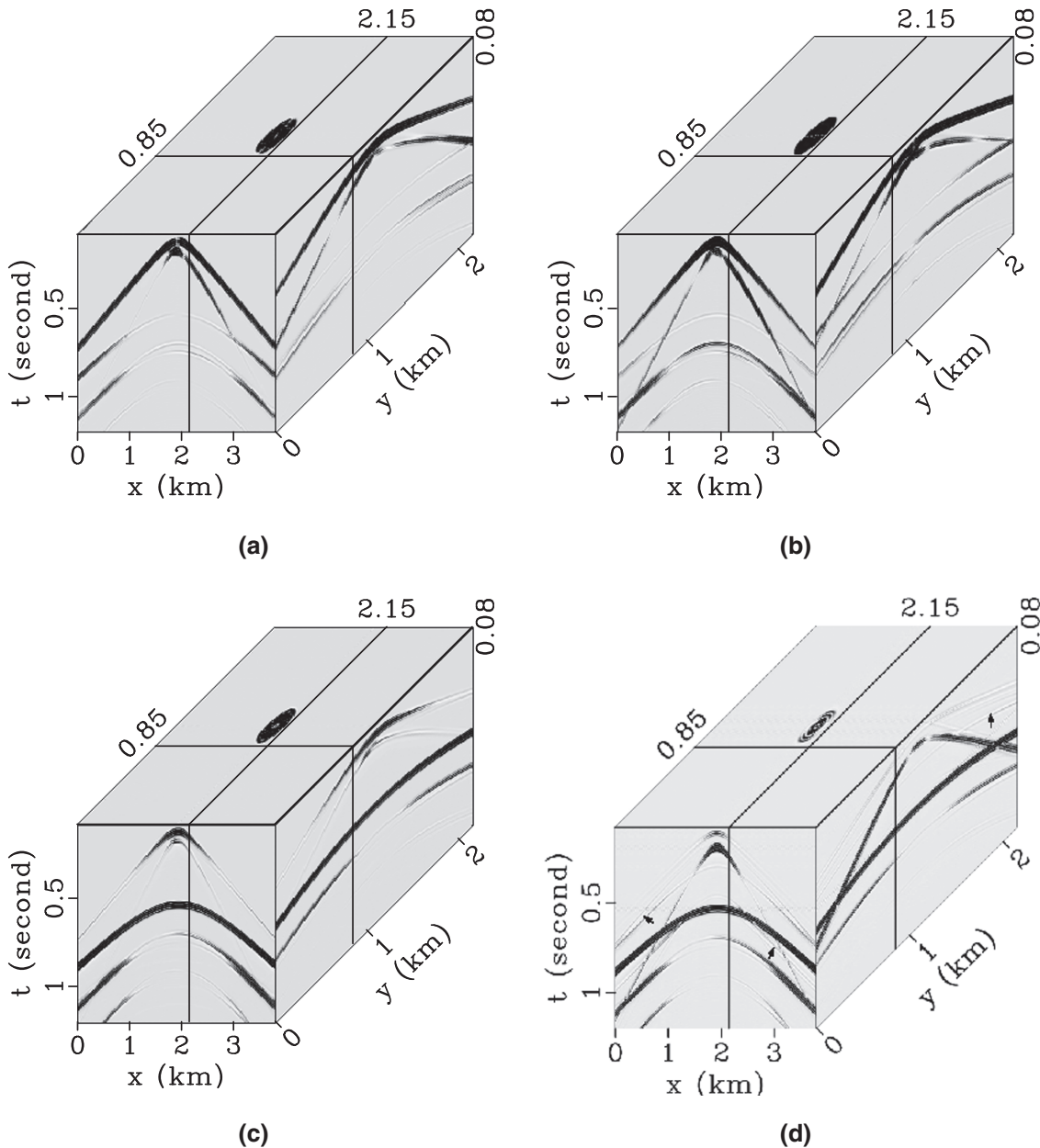


Figure 7 Three-component seismograms recorded on the surface of the monoclinic/orthorhombic model: (a) x -component, (b) y -component, and (c) z -component of RSG-PSM and (d) z -component of the non-staggered PSM. Both types of artefacts are obvious in the non-staggered PSM. Black arrows labelled the artificial reflection events associated with the second type of artefact. The RSG-PSM produced dispersion-free and artefacts invisible seismograms, and shear-wave splitting can be easily found at the reflection events.

or polarisation-based projection (Dellinger and Etgen 1990; Cheng and Fomel 2014). Interpolation in the space domain (Zhang and McMechan 2010) or phase shifts in the wavenumber domain (Firouzi *et al.* 2012) can be used to estimate the needed values at common grid points. This will lead to extra computational expenses. Fortunately, such additional

operations are not required for decomposing the wavefields synthesized by the rotated staggered-grid-based pseudo-spectral method because all the particle velocity components are defined at the same nodes with this grid configuration. We can exploit this advantage to develop efficient spectral methods to simultaneously extrapolate and decompose the

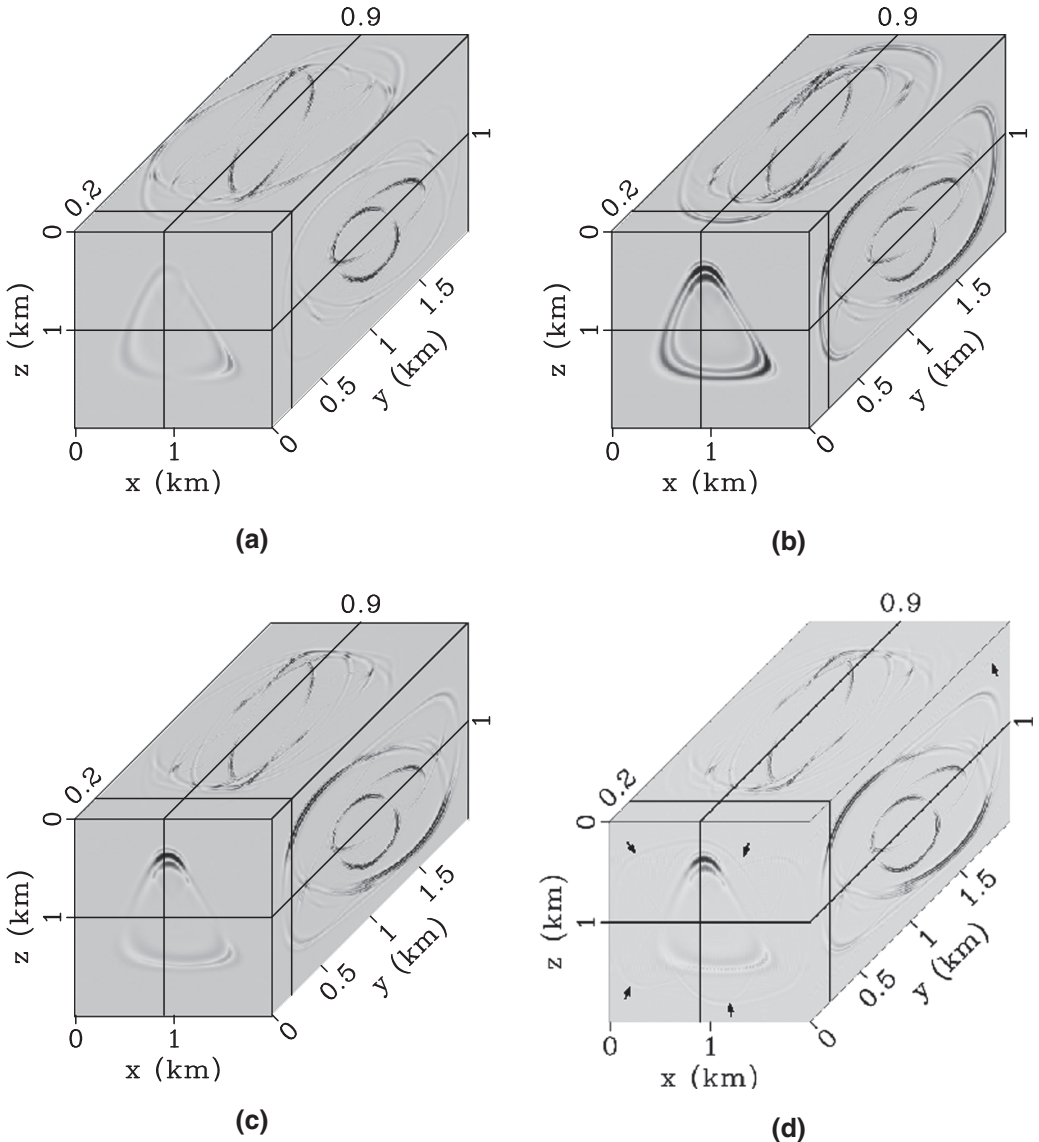


Figure 8 Elastic wavefields in a homogeneous triclinic medium at 0.35 seconds: (a) x -component, (b) y -component, and (c) z -component of RSG-PSM and (d) z -component of non-staggered PSM. All three types of waves (qP, qS1, and qS2) can be clearly identified, and the artefacts of the RSG-based PSM are invisible. The first type of ringing artefacts (labelled with black arrows) of the non-staggered PSM are still visible although they die down quickly in homogeneous media and cannot generate the second type of artefacts.

elastic wave modes, like in Cheng *et al.* (2016), Sun *et al.* (2016b), but on the base of velocity–stress equations for anisotropic media.

CONCLUSIONS

Grid staggering is essential for a pseudo-spectral method to suppress the non-causal ringing artefacts in simulating seismic wave propagation, but the standard implementation

can only be used to model anisotropy up to orthorhombic media. We have presented a pseudo-spectral method using the rotated staggered-grid configuration and compared with alternative remedies to the standard staggered-grid pseudo-spectral method (PSM). The theoretical derivation and numerical experiments show that the rotated staggered-grid-based PSM provides efficient solutions for high-quality elastic wave modelling in 2D and 3D anisotropic media with arbitrary symmetries. We expect that this novel full-wave modelling

technique has a great potential for seismic migration and waveform inversion in real anisotropic media such as the fractured gas shale formations.

ACKNOWLEDGEMENTS

The first author appreciates T. F. Wang, C. L. Wang, and W. J. He for their fruitful discussion in this study. The authors would like to thank the National Natural Science Foundation of China for the support under grants 41630964, 41474099, and 41674117. This publication is also based upon work supported by King Abdullah University of Science and Technology (KAUST) Office of Sponsored Research (OSR) under Award 2230. We appreciate the support of Madagascar open-source software for reproducible research (Fomel *et al.* 2013).

REFERENCES

- Bakulin A., Grechka V. and Tsvankin I. 2000a. Estimation of fracture parameters from reflection seismic data—Part I: HTI model due to a single fracture set. *Geophysics* **65**, 1788–1802.
- Bakulin A., Grechka V. and Tsvankin I. 2000b. Estimation of fracture parameters from reflection seismic data—Part II: Fractured models with orthorhombic symmetry. *Geophysics* **65**, 1803–1817.
- Bale R.A. 2002. Staggered grids for 3D pseudospectral modeling in anisotropic elastic media. *CREWES Research Report* **14**, 1–14.
- Bansal R. and Sen M. 2008. Finite-difference modeling of s-wave splitting in anisotropic media. *Geophysical Prospecting* **56**, 293–312.
- Bartolo L.D., Dors C. and Mansur W.J. 2015. Theory of equivalent staggered-grid schemes: application to rotated and standard grids in anisotropic media. *Geophysical Prospecting* **63**, 1–29.
- Benjemaa M., Glinsky-Olivier N., Cruz-Atienza V.M., Virieux J. and Piperno S. 2007. Dynamic non-planar crack rupture by a finite volume method. *Geophysical Journal International* **171**, 271–285.
- Carcione J.M. 1991. Domain decomposition for wave propagation problems. *Journal of Scientific Computing* **6**, 453–472.
- Carcione J.M. 1999. Staggered mesh for the anisotropic and viscoelastic wave equation. *Geophysics* **64**, 1863–1866.
- Carcione J.M. 2007. *Wave Fields in Real Media: Wave Propagation in Anisotropic, Anelastic, Porous and Electromagnetic Media*. Elsevier Ltd.
- Carcione J.M., Herman G.C. and Kroode A.P.E.T. 2002. Seismic modeling. *Geophysics* **67**, 1304–1325.
- Cheng J.B. and Fomel S. 2014. Fast algorithms of elastic wave mode separation and vector decomposition using low-rank approximation for anisotropic media. *Geophysics* **79**, C97–C110.
- Cheng J.B., Wu Z.D., Alkhalifah T., Zou P. and Wang C.L. 2016. Simulating propagation of decoupled elastic waves using low-rank approximate mixed-domain integral operators for anisotropic media. *Geophysics* **81**, T63–T77.
- Chung E. and Engquist B. 2006. Optimal discontinuous Galerkin methods for wave propagation. *SIAM Journal on Numerical Analysis* **44**, 2131–2158.
- Correa G.J., Spiegelman M., Carbotte S. and Mutter J.C. 2002. Centered and staggered Fourier derivatives and Hilbert transforms. *Geophysics* **67**, 1558–1563.
- De Basabe J.D., Sen M.K. and Wheeler M.F. 2008. The interior penalty discontinuous Galerkin method for elastic wave propagation: grid dispersion. *Geophysical Journal International* **175**, 83–93.
- Dellinger J. and Etgen J. 1990. Wave-type separation in 3-D anisotropic media. 59th SEG annual international meeting, Expanded Abstracts 977–979.
- Eriksson K. and Johnson C. 1991. Adaptive finite element methods for parabolic problems I: a linear model problem. *SIAM Journal on Numerical Analysis* **28**, 43–77.
- Firouzi K., Cox B.T., Treeby B.E. and Saffari N. 2012. A first-order k-space model for elastic wave propagation in heterogeneous media. *The Journal of the Acoustical Society of America* **132**, 1271–1283.
- Fomel S., Sava P., Vlad I., Liu Y. and Bashkardin V. 2013. Madagascar: open-source software project for multidimensional data analysis and reproducible computational experiments. *Journal of Open Research Software* **1**, e8.
- Fornberg B. 1987. The pseudospectral method: comparisons with finite differences for the elastic wave equation. *Geophysics* **52**, 483–501.
- Fornberg B. 1988. The pseudospectral method: accurate representation of interfaces in elastic wave calculations. *Geophysics* **53**, 625–637.
- Igel H., Mora P. and Riollet B. 1995. Anisotropic wave propagation through finite-difference grids. *Geophysics* **60**, 1203–1216.
- Klin P., Priolo E. and Seriani G. 2010. Numerical simulation of seismic wave propagation in realistic 3-D geo-models with a Fourier pseudo-spectral method. *Geophysical Journal International* **183**, 905–922.
- Komatitsch D., Barnes C. and Tromp J. 2000. Simulation of anisotropic wave propagation based on a spectral element method. *Geophysics* **65**, 1251–1260.
- Komatitsch D. and Martin R. 2007. An unsplit convolutional perfectly matched layer improved at grazing incidence for the seismic wave equation. *Geophysics* **72**, SM155–SM167.
- Kosloff D. and Baysal E. 1982. Forward modelling by a Fourier method. *Geophysics* **47**, 1402–1412.
- Lebedev V. 1964. Difference analogues of orthogonal decompositions of basic differential operators and some boundary value problems. I. *USSR Computational Mathematics and Mathematical Physics* **4**, 449–465.
- Lisitsa V. and Vishnevskiy D. 2010. Lebedev scheme for the numerical simulation of wave propagation in 3D anisotropic elasticity. *Geophysical Prospecting* **58**, 619–635.
- Lisitsa V. and Vishnevskiy D. 2011. On specific features of the Lebedev scheme in simulating elastic wave propagation in anisotropic media. *Numerical Analysis and Applications* **4**, 155–167.

- Lisitsa V., Tcheverda V. and Vishnevskiy D. 2012. Numerical simulation of seismic waves in models with anisotropic formations: coupling Virieux and Lebedev finite-difference schemes. *Computational Geosciences* **16**, 1135–1152.
- Liu Y. 2013. Globally optimal finite-difference schemes based on least squares. *Geophysics* **78**, T113–T132.
- Moczo P., Kristek J., Vavrycuk V., Vavrycuk R. and Halada L. 2002. 3D heterogeneous staggered-grid finite-difference modeling of seismic motion with volume harmonic and arithmetic averaging of elastic moduli and densities. *Bulletin of the Seismological Society of America* **92**, 3042–3066.
- Moczo P., Roberstsson O.A. and Eisner L. 2007. The finite-difference time-domain method for modeling of seismic wave propagation. In: *Advances in Wave Propagation in Heterogeneous Earth, Advances in Geophysics*, Vol. 48 (eds. R.S. Wu and V. Maupin), pp. 421–516.
- Mora P. 1986. Elastic finite difference with convolutional operators. *Stanford Exploration Project Report* **48**, 277–289.
- Operto S., Virieux J., Ribodetti A. and Anderson J.E. 2009. Finite-difference frequency-domain modeling of viscoacoustic wave propagation in 2D tilted transversely isotropic (TTI) media. *Geophysics* **74**, T75–T95.
- Ozdenvar T. and McMechan G. 1996. Causes and reduction of numerical artifacts in pseudo-spectral wavefield extrapolation. *Geophysical Journal International* **126**, 819–829.
- Roberstsson J.O. 1996. A numerical free-surface condition for elastic-viscoelastic finite-difference modeling in the presence of topography. *Geophysics* **61**, 1921–1934.
- Saenger E.H., Gold N. and Shapiro S.A. 2000. Modeling the propagation of the elastic waves using a modified finite-difference grid. *Wave Motion* **31**, 77–92.
- Schoenberg M. 1980. Elastic wave behavior across linear slip interfaces. *The Journal of the Acoustical Society of America* **68**, 1516–1521.
- Sun J., Fomel S. and Ying L. 2016a. Low-rank one-step wave extrapolation for reverse time migration. *Geophysics* **81**, S39–S54.
- Sun J., Fomel Y.S.S. and Fowler P. 2016b. Recursive integral time extrapolation of elastic waves using lowrank approximation. 86th SEG annual international meeting, Expanded Abstracts 4145–4151.
- Tessmer E. 1995. 3-D seismic modelling of general material anisotropy in the presence of the free surface by a Chebyshev spectral method. *Geophysical Journal International* **121**, 557–575.
- Virieux J. 1984. SH-wave propagation in heterogeneous media: velocity-stress finite-difference method. *Geophysics* **49**, 1933–1957.
- Virieux J., Calandra H. and Plessix R. 2011. A review of the spectral, pseudo-spectral, finite-difference and finite-element modelling techniques for geophysical imaging. *Geophysical Prospecting* **59**, 794–813.
- Wang C.L., Cheng J.B. and Arntsen B. 2016. Scalar and vector imaging based on wave mode decoupling for elastic reverse time migration in isotropic and transversely isotropic media. *Geophysics* **81**, S383–S398.
- Wang T.F. and Cheng J.B. 2016. Elastic full-waveform inversion based on mode decomposition: the approach and mechanism. *Geophysical Journal International* in press.
- Wang T.F. and Cheng J.B. 2017. Elastic full waveform inversion based on mode decomposition: the approach and mechanism. *Geophysical Journal International* **209**, 606–622.
- Wang Y. and Takenaka H. 2001. A multidomain approach of the Fourier pseudospectral method using discontinuous grid for elastic wave modeling. *Earth, Planets and Space* **53**, 149–158.
- Yan J. and Sava P. 2008. Isotropic angle domain elastic reverse time migration. *Geophysics* **73**, S229–S239.
- Yang D.H., Wang L. and Deng X.Y. 2010. An explicit split-step algorithm of the implicit Adams method for solving 2-D acoustic and elastic wave equations. *Geophysical Journal International* **180**, 291–310.
- Zhang J.F. and Liu T. 1999. P-SV-wave propagation in heterogeneous media: grid method. *Geophysical Journal International* **136**, 431–438.
- Zhang Q. and McMechan G.A. 2010. 2D and 3D elastic wavefield vector decomposition in the wavenumber domain for VTI media. *Geophysics* **75**, D13–D26.

APPENDIX A: STAGGERED-GRID PSEUDO-SPECTRAL METHOD USING STIFFNESS MATRIX DECOMPOSITION

For anisotropy with lower symmetries than orthorhombic or when the symmetry axis is not aligned with the grid, we have to use shift operators to relocate strain components prior to the multiplication by the stiffness coefficients. Applications of these operators have important consequences on the elements of the stiffness matrix that present to symmetry systems lower than orthorhombic (more than nine independent elastic constants).

Therefore, Bale (2002) suggested decomposing the stiffness matrix into aligned (orthorhombic) and non-aligned (non-orthorhombic) parts as follows:

$$\mathbf{C}_{stag} = \mathbf{C}_{ort} + \mathbf{S}^+ \mathbf{C}_{non} \mathbf{S}^-, \quad (\text{A-1})$$

with

$$\mathbf{C}_{ort} = \begin{bmatrix} C_{11} & C_{12} & C_{13} & 0 & 0 & 0 \\ C_{12} & C_{22} & C_{23} & 0 & 0 & 0 \\ C_{13} & C_{23} & C_{33} & 0 & 0 & 0 \\ 0 & 0 & 0 & C_{44} & 0 & 0 \\ 0 & 0 & 0 & 0 & C_{55} & 0 \\ 0 & 0 & 0 & 0 & 0 & C_{66} \end{bmatrix},$$

$$\mathbf{C}_{non} = \begin{bmatrix} 0 & 0 & 0 & C_{14} & C_{15} & C_{16} \\ 0 & 0 & 0 & C_{24} & C_{25} & C_{26} \\ 0 & 0 & 0 & C_{34} & C_{35} & C_{36} \\ C_{14} & C_{24} & C_{34} & 0 & C_{45} & C_{46} \\ C_{15} & C_{25} & C_{35} & C_{45} & 0 & C_{56} \\ C_{16} & C_{26} & C_{36} & C_{46} & C_{56} & 0 \end{bmatrix},$$

and

$$\mathbf{S}^{\pm} = \begin{bmatrix} 1 & 0 & 0 & 0 & 0 & 0 \\ 0 & 1 & 0 & 0 & 0 & 0 \\ 0 & 0 & 1 & 0 & 0 & 0 \\ 0 & 0 & 0 & S_y^{\pm} S_z^{\pm} & 0 & 0 \\ 0 & 0 & 0 & 0 & S_x^{\pm} S_z^{\pm} & 0 \\ 0 & 0 & 0 & 0 & 0 & S_x^{\pm} S_y^{\pm} \end{bmatrix},$$

in which S_x^{\pm} , S_y^{\pm} , and S_z^{\pm} denote the forward and backward shift operators along the x -, y -, and z -axes, respectively. For instance

$$S_x^{\pm} \phi = \sum_{k_x=0}^{k_x(N)} s_x^{\pm} \cdot \tilde{\phi}(k_x) \exp(ik_x x). \quad (\text{A-2})$$

Based upon equation (2), the diagonal matrices \mathbf{S}^{\pm} can be applied as pre- and post-multipliers to handle the non-aligned terms as follows. (a) Multiply the strain vector by \mathbf{C}_{ort} using the staggered mesh defined in Fig. 1. This yields the “aligned” stress vector without any shift operations. (b) Pre-multiply the strain vector by \mathbf{S}^{-} , which means mapping all strains to regular node (i, j, k) . Then multiply by \mathbf{C}_{non} to determine “non-aligned” stress at those nodes, followed by post-multiplying the stress vector by \mathbf{S}^{+} to relocate them to the intergrid nodes. This eventually yields the “non-aligned” stress vector. (c) Sum the “aligned” and “non-aligned” stress vectors to get the total stress. Taking the calculation of off-diagonal stress τ_{yz} as an example (see Fig. 1), we have to shift $(\partial_x v_z + \partial_z v_x)$ from intergrid node ∇ to regular node \blacklozenge using S_x^- followed by S_z^- and then shift the multiplication $C_{45}(\partial_x v_z + \partial_z v_x)$ from regular node \blacklozenge to intergrid node Δ (i.e., location of τ_{yz}) using S_z^+ followed by S_y^+ . Note that the shift operator \mathbf{S}^- can be merged into the spectral derivative operator whereas \mathbf{S}^+ cannot.

APPENDIX B: STAGGERED-GRID PSEUDO-SPECTRAL METHOD USING THE LEBEDEV GRID

The Lebedev grid (Lebedev 1964) define all components of particle velocity on one staggered grid and all components of stress and strain at another staggered grid. We can apply it to pseudo-spectral modelling for avoiding the non-causal ringing artefacts in arbitrary anisotropic media.

Following Lisitsa and Vishnevskiy (2010), we use four sets of variables (for 3D problems) at different locations of an elementary grid cell to assist staggering between stress and particle velocity components. As illustrated in Fig. B-1, the

four non-intersecting stress sets, i.e., τ^1 , τ^2 , τ^3 , and τ^4 , are defined at the corner of the cell and at the centre of the cube faces, whereas the four non-intersecting particle velocity sets, i.e., v^1 , v^2 , v^3 , and v^4 , are defined at the centre of the cell and halfway between the corners. Accordingly, we solve the velocity–stress wave equations using the staggered spectral operators (e.g., equation (4)) on the four non-intersecting grid sets. In other words, we solve the following four sets of particle velocity motion equations:

$$\begin{aligned} \rho \partial_t v_x^1 &= D_x^- \tau_{xx}^1 + D_y^+ \tau_{xy}^2 + D_z^+ \tau_{xz}^3, \\ \rho \partial_t v_y^1 &= D_x^- \tau_{xy}^1 + D_y^+ \tau_{yy}^2 + D_z^+ \tau_{yz}^3, \\ \rho \partial_t v_z^1 &= D_x^- \tau_{xz}^1 + D_y^+ \tau_{yz}^2 + D_z^+ \tau_{zz}^3, \end{aligned} \quad (\text{B-1})$$

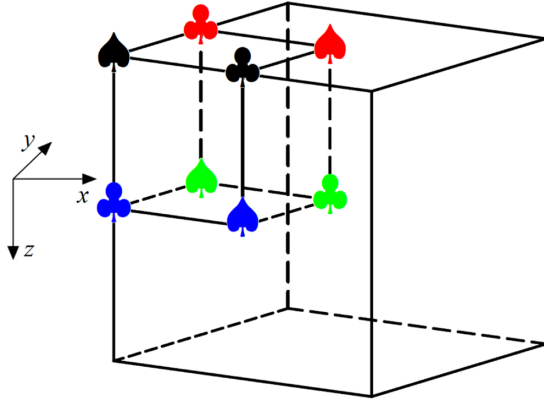
$$\begin{aligned} \rho \partial_t v_x^2 &= D_x^+ \tau_{xx}^2 + D_y^- \tau_{xy}^1 + D_z^+ \tau_{xz}^4, \\ \rho \partial_t v_y^2 &= D_x^+ \tau_{xy}^2 + D_y^- \tau_{yy}^1 + D_z^+ \tau_{yz}^4, \\ \rho \partial_t v_z^2 &= D_x^+ \tau_{xz}^2 + D_y^- \tau_{yz}^1 + D_z^+ \tau_{zz}^4, \end{aligned} \quad (\text{B-2})$$

$$\begin{aligned} \rho \partial_t v_x^3 &= D_x^+ \tau_{xx}^3 + D_y^- \tau_{xy}^4 + D_z^- \tau_{xz}^1, \\ \rho \partial_t v_y^3 &= D_x^+ \tau_{xy}^3 + D_y^- \tau_{yy}^4 + D_z^- \tau_{yz}^1, \\ \rho \partial_t v_z^3 &= D_x^+ \tau_{xz}^3 + D_y^- \tau_{yz}^4 + D_z^- \tau_{zz}^1, \end{aligned} \quad (\text{B-3})$$

$$\begin{aligned} \rho \partial_t v_x^4 &= D_x^- \tau_{xx}^4 + D_y^- \tau_{xy}^3 + D_z^- \tau_{xz}^2, \\ \rho \partial_t v_y^4 &= D_x^- \tau_{xy}^4 + D_y^- \tau_{yy}^3 + D_z^- \tau_{yz}^2, \\ \rho \partial_t v_z^4 &= D_x^- \tau_{xz}^4 + D_y^- \tau_{yz}^3 + D_z^- \tau_{zz}^2, \end{aligned} \quad (\text{B-4})$$

and the four sets of the stress–strain relationship

$$\begin{bmatrix} \partial_t \tau_{xx}^1 \\ \partial_t \tau_{yy}^1 \\ \partial_t \tau_{zz}^1 \\ \partial_t \tau_{yz}^1 \\ \partial_t \tau_{xz}^1 \\ \partial_t \tau_{xy}^1 \end{bmatrix} = \begin{bmatrix} C_{11} & C_{12} & C_{13} & C_{14} & C_{15} & C_{16} \\ C_{12} & C_{22} & C_{23} & C_{24} & C_{25} & C_{26} \\ C_{13} & C_{23} & C_{33} & C_{34} & C_{35} & C_{36} \\ C_{14} & C_{24} & C_{34} & C_{44} & C_{45} & C_{46} \\ C_{15} & C_{25} & C_{35} & C_{45} & C_{55} & C_{56} \\ C_{16} & C_{26} & C_{36} & C_{46} & C_{56} & C_{66} \end{bmatrix} \times \begin{bmatrix} D_x^+ v_x^1 \\ D_y^+ v_y^2 \\ D_z^+ v_z^3 \\ D_z^- v_y^3 + D_y^- v_z^2 \\ D_z^+ v_x^3 + D_x^- v_z^1 \\ D_x^- v_y^1 + D_y^- v_x^2 \end{bmatrix}, \quad (\text{B-5})$$



	(i, j, k)	τ^1
	$(i + \frac{1}{2}, j, k)$	v^1
	$(i + \frac{1}{2}, j + \frac{1}{2}, k)$	τ^2
	$(i, j + \frac{1}{2}, k)$	v^2
	$(i + \frac{1}{2}, j, k + \frac{1}{2})$	τ^3
	$(i, j, k + \frac{1}{2})$	v^3
	$(i, j + \frac{1}{2}, k + \frac{1}{2})$	τ^4
	$(i + \frac{1}{2}, j + \frac{1}{2}, k + \frac{1}{2})$	v^4

Figure B-1 Lebedev grid configuration for 3D elastic wave modelling.

$$\begin{bmatrix} \partial_t \tau_{xx}^2 \\ \partial_t \tau_{yy}^2 \\ \partial_t \tau_{zz}^2 \\ \partial_t \tau_{yz}^2 \\ \partial_t \tau_{xz}^2 \\ \partial_t \tau_{xy}^2 \end{bmatrix} = \begin{bmatrix} C_{11} & C_{12} & C_{13} & C_{14} & C_{15} & C_{16} \\ C_{12} & C_{22} & C_{23} & C_{24} & C_{25} & C_{26} \\ C_{13} & C_{23} & C_{33} & C_{34} & C_{35} & C_{36} \\ C_{14} & C_{24} & C_{34} & C_{44} & C_{45} & C_{46} \\ C_{15} & C_{25} & C_{35} & C_{45} & C_{55} & C_{56} \\ C_{16} & C_{26} & C_{36} & C_{46} & C_{56} & C_{66} \end{bmatrix} \times \begin{bmatrix} D_x^- v_x^2 \\ D_y^- v_y^1 \\ D_z^+ v_z^4 \\ D_z^+ v_y^4 + D_y^- v_z^1 \\ D_z^- v_x^4 + D_x^- v_z^2 \\ D_x^- v_y^2 + D_y^- v_x^1 \end{bmatrix}, \quad (B-6)$$

$$\begin{bmatrix} \partial_t \tau_{xx}^4 \\ \partial_t \tau_{yy}^4 \\ \partial_t \tau_{zz}^4 \\ \partial_t \tau_{yz}^4 \\ \partial_t \tau_{xz}^4 \\ \partial_t \tau_{xy}^4 \end{bmatrix} = \begin{bmatrix} C_{11} & C_{12} & C_{13} & C_{14} & C_{15} & C_{16} \\ C_{12} & C_{22} & C_{23} & C_{24} & C_{25} & C_{26} \\ C_{13} & C_{23} & C_{33} & C_{34} & C_{35} & C_{36} \\ C_{14} & C_{24} & C_{34} & C_{44} & C_{45} & C_{46} \\ C_{15} & C_{25} & C_{35} & C_{45} & C_{55} & C_{56} \\ C_{16} & C_{26} & C_{36} & C_{46} & C_{56} & C_{66} \end{bmatrix} \times \begin{bmatrix} D_x^+ v_x^4 \\ D_y^- v_y^3 \\ D_z^- v_z^2 \\ D_z^- v_y^2 + D_y^- v_z^3 \\ D_z^- v_x^2 + D_x^+ v_z^4 \\ D_x^+ v_y^4 + D_y^- v_x^3 \end{bmatrix}, \quad (B-8)$$

$$\begin{bmatrix} \partial_t \tau_{xx}^3 \\ \partial_t \tau_{yy}^3 \\ \partial_t \tau_{zz}^3 \\ \partial_t \tau_{yz}^3 \\ \partial_t \tau_{xz}^3 \\ \partial_t \tau_{xy}^3 \end{bmatrix} = \begin{bmatrix} C_{11} & C_{12} & C_{13} & C_{14} & C_{15} & C_{16} \\ C_{12} & C_{22} & C_{23} & C_{24} & C_{25} & C_{26} \\ C_{13} & C_{23} & C_{33} & C_{34} & C_{35} & C_{36} \\ C_{14} & C_{24} & C_{34} & C_{44} & C_{45} & C_{46} \\ C_{15} & C_{25} & C_{35} & C_{45} & C_{55} & C_{56} \\ C_{16} & C_{26} & C_{36} & C_{46} & C_{56} & C_{66} \end{bmatrix} \times \begin{bmatrix} D_x^- v_x^3 \\ D_y^+ v_y^4 \\ D_z^- v_z^1 \\ D_z^- v_y^1 + D_y^+ v_z^4 \\ D_z^- v_x^1 + D_x^- v_z^3 \\ D_x^- v_y^3 + D_y^+ v_x^4 \end{bmatrix}, \quad (B-7)$$

In this context, a point source cannot be introduced at a single grid point and requires special treatment (Lisitsa and Vishnevskiy 2010). A natural way to store the medium parameters is to define them within each elementary grid cell, i.e., at the corners of the cell. This implies that the medium parameters needed at other staggered nodes should be obtained from the defined parameters at the corners, e.g., Moczo *et al.* (2002). The elimination of artificial solutions directly uses the method for the Lebedev grid-based finite-difference method proposed by Lisitsa and Vishnevskiy (2011).